

Global hybrid simulations of energetic particle effects on the $n=1$ mode in tokamaks: Internal kink and fishbone instability

G. Y. Fu and W. Park

Princeton Plasma Physics Laboratory, Princeton, New Jersey 08543

H. R. Strauss

New York University, New York, New York 10012

J. Breslau, J. Chen, and S. Jardin

Princeton Plasma Physics Laboratory, Princeton, New Jersey 08543

L. E. Sugiyama

Massachusetts Institute of Technology, Cambridge, Massachusetts 02139

(Received 19 July 2005; accepted 18 April 2006; published online 24 May 2006)

Global hybrid simulations of energetic particle effects on the $n=1$ internal kink mode have been carried out for tokamaks. For the International Thermonuclear Experimental Reactor (ITER) [ITER Physics Basis Editors *et al.*, Nucl. Fusion **39**, 2137 (1999)], it is shown that alpha particle effects are stabilizing for the internal kink mode. However, the elongation of ITER reduces the stabilization effects significantly. Nonlinear simulations of the precessional drift fishbone instability for circular tokamak plasmas show that the mode saturates due to flattening of the particle distribution function near the resonance region. The mode frequency chirps down rapidly as the flattening region expands radially outward. Fluid nonlinearity reduces the saturation level. © 2006 American Institute of Physics. [DOI: 10.1063/1.2203604]

I. INTRODUCTION

As we approach burning plasma experiments such as the International Thermonuclear Experimental Reactor (ITER),¹ the physics of energetic particles is an area of increasing importance. A key issue is how energetic alpha particles would affect the bulk plasmas and whether alpha-driven magnetohydrodynamics (MHD) instabilities will induce large alpha particle transport and associated losses. To answer this question, we need comprehensive numerical simulations which can predict alpha particle-driven instabilities in the new parameter regimes of burning plasmas. Toward this end, we have developed a particle/MHD hybrid code, M3D,² to study the physics of energetic particle-driven instabilities in present and future fusion devices. In this work, we focus on energetic particle effects on the $n=1$ kink mode (where n is the toroidal mode number), namely, alpha particle stabilization of the internal kink mode in ITER and the nonlinear dynamics of energetic particle-driven fishbone instability in tokamaks.

The M3D code contains multiple levels of physics models including resistive MHD, two fluids,³ and particle/MHD hybrid. In the present work, the particle/MHD hybrid model is used. In this model, the plasma is divided into two parts: the bulk plasma (thermal electrons and ions) and the energetic particles. The bulk plasma is treated as a single fluid whereas the energetic particles are treated either as drift-kinetic or gyrokinetic particles. The details of the model are described in the next section.

The original version of the M3D hybrid code has been applied to study nonlinear saturation of energetic particle-driven toroidal Alfvén eigenmodes,⁴ stabilization of the internal kink mode and the excitation of the fishbone

instability.² Recently, we have extended the hybrid level of M3D code to general three-dimensional (3D) meshes by using linear finite elements in the poloidal planes and finite differences in the toroidal direction.⁵ These new capabilities have enabled us to study energetic particle-driven modes in many types of fusion devices including shaped tokamaks such as ITER, spherical tokamaks,⁶ and stellarators.⁷ In this work, we present results on alpha particle stabilization of internal kink mode in ITER and on the nonlinear evolution of the fishbone instability.

The energetic particle stabilization of the internal kink mode has been studied extensively. The stabilization comes from conservation of the third invariant when the energetic particle precession frequency is much larger than the MHD growth rate.^{8,9} Most previous work^{10–13} used analytic methods valid for large aspect ratio circular tokamaks. General shaped tokamak equilibria have been considered in a few studies only.^{14–16} In this work, we consider alpha particle stabilization of the internal kink in ITER. In particular, we study shaping effects on the alpha stabilization. We find that the elongation of ITER significantly reduces the stabilization compared to that of an equivalent tokamak with circular cross section.

On the second topic of this article, we have carried out extensive nonlinear simulations of the fishbone instability driven by energetic particles in tokamaks. The fishbone is an $n=1$ internal mode with dominant poloidal mode number $m=1$ which is resonantly destabilized by energetic trapped particles. It was first discovered¹⁷ in the Princeton tokamak divertor experiments (PDX) in 1980. The name came from its characteristic shape of the Mirnov magnetic signal. Since then, the instability has been observed in many tokamaks and

stellarators. Extensive theoretical work has been done over the years. There were two early competing theories to explain the experimental observations. Chen *et al.*¹⁸ proposed that the mode is destabilized by energetic trapped ions via precessional drift resonance ($\omega = \omega_d$) and that the mode is intrinsically an energetic particle mode. Coppi *et al.*¹⁹ proposed that the mode is MHD-like with a frequency on the order of the thermal ion's diamagnetic drift frequency ($\omega = \omega_{*i}$). More recently, the possibility of a fishbone instability driven by the bounce resonance has also been proposed.²⁰ Finally, there is the possibility of the fishbone being driven by circulating particles.²¹ In this work, we focus on the precessional drift branch due to its interesting nonlinear behavior.

Compared to linear theory, the nonlinear theory of the fishbone is less mature. Early work used phenomenological predator-prey models^{18,22,23} to explain the mode saturation and bursting due to resonant particle loss. More recently, Candy *et al.*²⁴ simulated a full cycle of fishbone oscillations by using a simplified hybrid model where a fixed internal kink mode structure was used. The fluid nonlinearity was neglected and the mode saturation was due entirely to the particle nonlinearity. On the other hand, Odblom *et al.*²⁵ investigated the fluid nonlinearity of the fishbone instability while neglecting the particle nonlinearity. They found that the fluid nonlinearity enhances the initial growth rate near marginal stability. In this work, we use a fully self-consistent model which includes both particle and fluid nonlinearities. The mode structure is determined nonperturbatively both in the linear and nonlinear regime including energetic particle effects. We find that the nonlinear dynamics is mainly determined by the particle nonlinearity. The mode saturates due to flattening of the particle distribution in the resonance region. The mode frequency chirps down significantly as the width of flattening region increases. The fluid nonlinearity is found to reduce the saturation level.

This article is organized as follows: Sec. II describes the hybrid model used in this work; Sec. III describes the benchmarking of the M3D hybrid code; Sec. IV describes the results for alpha particle stabilization of the internal kink mode in ITER; Sec. V describes the results of nonlinear simulations of the fishbone instability; and finally, conclusions are given in Sec. VI.

II. PARTICLE/MHD HYBRID MODEL

In this work, we use a particle/MHD hybrid model to describe the interaction of energetic particles and MHD waves. In the model,² the plasma is divided into two parts: the thermal component and the energetic particle component. The thermal ions and electrons are treated as a single fluid. The energetic species is treated as drift-kinetic particles or gyrokinetic particles. The energetic particle effects enter through the particle stress tensor \mathbf{P}_h in the momentum equation:

$$\rho \frac{d\mathbf{v}}{dt} = -\nabla P - \nabla \cdot \mathbf{P}_h + \mathbf{J} \times \mathbf{B}. \quad (1)$$

Equation (1) is closed by the Maxwell equations

$$\mathbf{J} = \nabla \times \mathbf{B}, \quad \frac{\partial \mathbf{B}}{\partial t} = -\nabla \times \mathbf{E}, \quad (2)$$

Ohm's law

$$\mathbf{E} + \mathbf{v} \times \mathbf{B} = \eta \mathbf{J}, \quad (3)$$

continuity equation for plasma mass density

$$d\rho/dt = -\rho \nabla \cdot \mathbf{v}, \quad (4)$$

and the pressure equation for thermal species

$$dP/dt = -\gamma P \nabla \cdot \mathbf{v}. \quad (5)$$

The particle stress tensor is taken to be in the Chew-Goldberger-Low (CGL) form

$$\mathbf{P}_h = P_\perp \mathbf{I} + (P_\parallel - P_\perp) \mathbf{b}\mathbf{b}, \quad (6)$$

where the parallel and perpendicular pressure is calculated from the particle distribution function F in the gyrocenter coordinates $(\mathbf{X}, v_\parallel, \mu)$:

$$P_\parallel(\mathbf{x}) = \int M v_\parallel^2 \delta(\mathbf{x} - \mathbf{X} - \rho_h) F(\mathbf{X}, v_\parallel, \mu) d^3\mathbf{X} dv_\parallel d\mu d\theta, \quad (7)$$

$$P_\perp(\mathbf{x}) = \int \frac{1}{2} M v_\perp^2 \delta(\mathbf{x} - \mathbf{X} - \rho_h) F(\mathbf{X}, v_\parallel, \mu) d^3\mathbf{X} dv_\parallel d\mu d\theta,$$

where $\rho_h = \mathbf{v}_\perp \times \mathbf{b} / \Omega$ is the gyroradius vector, (\mathbf{x}, \mathbf{v}) is the particle physical space coordinates, μ is the magnetic moment, and θ is the gyroangle.

The gyrocenter distribution F is represented by an ensemble of markers as

$$F = F(\mathbf{X}, v_\parallel, \mu) = \sum_i \delta(\mathbf{X} - \mathbf{X}_i) \delta(v_\parallel - v_{\parallel,i}) \delta(\mu - \mu_i). \quad (8)$$

The marker's orbits follow from the gyrokinetic equations:

$$\frac{d\mathbf{X}}{dt} = \frac{1}{B^{**}} \left[v_\parallel \left(\mathbf{B}^* - \mathbf{b}_0 \times \left(\langle \mathbf{E} \rangle - \frac{1}{e} \mu \nabla (B_0 + \langle \delta B \rangle) \right) \right) \right], \quad (9)$$

$$m \frac{dv_\parallel}{dt} = \frac{e}{B^{**}} \mathbf{B}^* \cdot \left(\langle \mathbf{E} \rangle - \frac{1}{e} \mu \nabla (B_0 + \langle \delta B \rangle) \right). \quad (10)$$

Here \mathbf{E} is the total electric field, \mathbf{B} is the total magnetic field, \mathbf{b}_0 is the unit vector in the direction of the equilibrium magnetic field, and B_0 and δB are the equilibrium and perturbed magnetic field, respectively. Note that the angular brackets represent gyro-average. The variables \mathbf{B}^* and B^{**} are given by

$$\mathbf{B}^* = \mathbf{B}_0 + \langle \delta \mathbf{B} \rangle + \frac{m v_\parallel}{q} \nabla \times \mathbf{b}_0, \quad B^{**} = \mathbf{B}^* \cdot \mathbf{b}_0. \quad (11)$$

The system of coupled equations (1) and (11) is a complete nonlinear particle/MHD hybrid model. The coupled equations are solved as an initial value problem. The δf method is used for the energetic particles. More details of the δf method and the particle part of the code are given in the appendices.

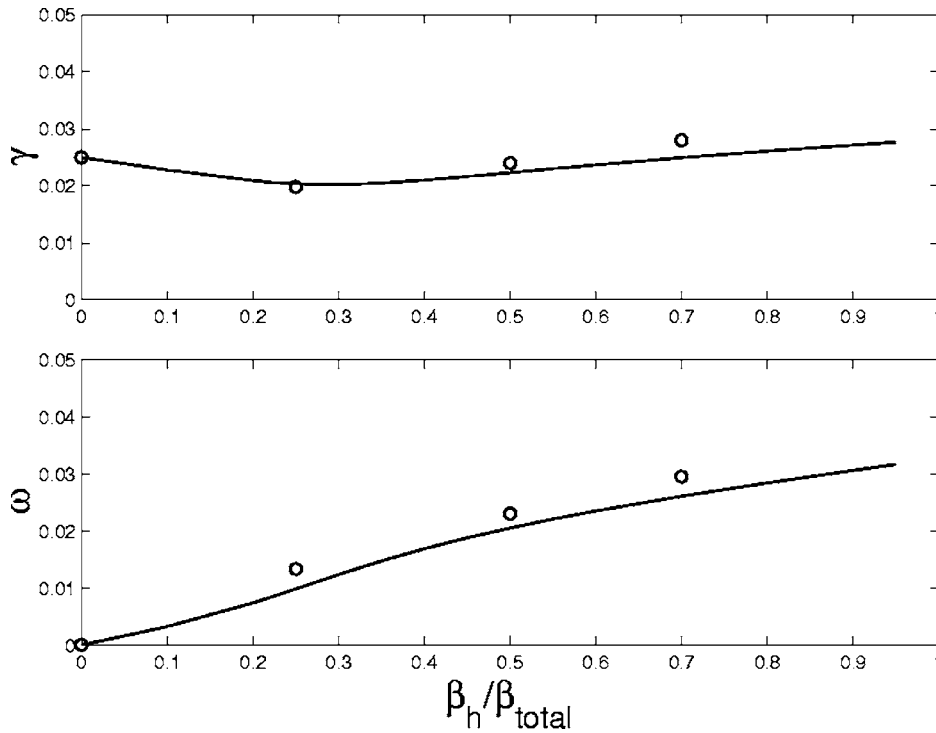


FIG. 1. The growth rate (top) and frequency (bottom) of the $n=1$ mode as a function of energetic particle beta fraction.

It should be noted that the gyrokinetic equations [Eq. (9)] reduce to the drift kinetic equations without gyro-average. For simplicity, all results presented here are obtained using the drift kinetic model.

Finally, we note that similar hybrid models have been used by others in the simulations of energetic particle-driven toroidal Alfvén eigenmodes.^{26,27}

III. BENCHMARKING OF THE M3D HYBRID CODE

The hybrid code M3D has been benchmarked extensively for both single particle orbits and collective effects of energetic particles on internal kink mode, fishbone instability and toroidal Alfvén eigenmodes. In particular, the new version of the code with unstructured mesh has been benchmarked against the original Fourier version of M3D.² For single particle orbits in tokamak equilibria, the particle energy and toroidal angular momentum are well conserved. The calculated linear TAE mode frequencies and growth rates agree well with those of the perturbative kinetic MHD linear eigenvalue code NOVA-K.²⁸ For a tokamak equilibrium, the results of M3D agree well with the NOVA2¹⁴ code for an $n=1$ internal kink mode and fishbone mode. Figure 1 compares the $n=1$ mode frequency and growth rates of NOVA2 and M3D as a function of the energetic particle beta at the center of plasma. We note that the agreement is quite good. The small difference could be caused by differences in the models. The NOVA2 code is a nonperturbative version of the NOVA-K code which only includes the trapped particle response of the precessional resonance in the limit of zero orbit width. The M3D code includes all wave particle resonances for both trapped and passing particles and full drift orbits. As the trapped particle precessional resonance is the dominant response of energetic particles, we expect the differences in the models are not important, as confirmed by Fig. 1. The results are

obtained for a circular tokamak with aspect ratio $R/a = 2.763$, total central beta $\beta_{\text{total}}(0) = 8.0\%$. The plasma density profile is uniform and the bulk plasma pressure profile is given by $P(\Psi) = P(0)\exp(-\Psi/0.25)$, where Ψ is the normalized poloidal flux variable with $\Psi=0$ at the center and $\Psi=1$ at the edge of the plasma. The safety factor profile is given by

$$q = q_0 + \Psi \left[q_1 - q_0 + (q'_1 - q_1 + q_0) \frac{(1 - \Psi_s)(\Psi - 1)}{\Psi - \Psi_s} \right], \quad (12)$$

where $\Psi_s = (q'_1 - q_1 + q_0)/(q'_0 + q'_1 - 2q_1 + 2q_0)$, $q_0 = 0.6$, $q_1 = 2.5$, $q'_0 = 0.78$, and $q'_1 = 5.0$. An isotropic slowing-down distribution is used for energetic particles and is given by

$$f = \frac{cH(v_0 - v)}{v^3 + v_c^3} \exp(-\langle \Psi \rangle / 0.25), \quad (13)$$

where v_0 is the maximum particle speed, $v_c = 0.58v_0$ is the critical velocity, c is a normalization factor, and $\langle \Psi \rangle$ is Ψ averaged over the particle orbit. As the toroidal angular momentum $P_\phi = e\Psi + Mv_\parallel RB_\phi/B$ is conserved, we can write

$$\langle \Psi \rangle = P_\phi / e - \frac{M}{e} \left\langle v_\parallel R \frac{B_\phi}{B} \right\rangle, \quad (14)$$

where e is the particle charge and M is the mass. For simplicity, we make use of the approximations

$$\left\langle v_\parallel R \frac{B_\phi}{B} \right\rangle \approx 0 \quad (15)$$

for trapped particles and

$$\left\langle v_{\parallel} R \frac{B_{\phi}}{B} \right\rangle \approx \text{sign}(v_{\parallel}) \sqrt{1 - \mu B_0 / E R_0} \quad (16)$$

for passing particles, with B_0 and R_0 being the magnetic field strength and major radius at the magnetic axis. Finally, the normalized particle gyroradius and speed is given by $\rho_h = v_0 / (\Omega_{ch} a) = 0.0125$ and $v_0 / v_A = 4$ where $\Omega_{ch} = e B_0 / (M c)$ is the energetic particle's cyclotron frequency.

IV. ALPHA PARTICLE STABILIZATION OF INTERNAL KINK MODE IN ITER

We now consider the effects of fusion alpha particles on the stability of the internal kink mode in burning plasmas. Specifically, we consider parameters and profiles of ITER. It is well known that energetic particles such as high energy alpha particles have a significant stabilization effect on the internal kink mode. There have been many previous studies related to this physics. However, most of the previous work assumed large aspect ratio and circular flux surfaces. Here, we apply the M3D hybrid code, which can treat arbitrary aspect ratio and shaped plasma cross sections. We find that cross section elongation is an important effect for the alpha particle stabilization of the internal kink.

The alpha particle stabilization of the internal kink can be described in the limit of small alpha particle beta as follows:

$$\frac{\gamma}{\omega_A} = \frac{\gamma_{\text{MHD}}}{\omega_A} - \beta_{\alpha}(0) \delta W_{\alpha}, \quad (17)$$

here ω_A is the shear Alfvén frequency, γ is the net growth rate, γ_{MHD} is the MHD growth rate including alpha's pressure effects, $\beta_{\alpha}(0)$ is the central alpha beta, and δW_{α} is an order of unity numerical factor which represents the stabilizing effects of alpha particle's nonadiabatic response. δW_{α} can be derived from a quadratic form and is written as follows:

$$\beta_{\alpha}(0) \delta W_{\alpha} = - \frac{1}{\delta I} \frac{R_0^2}{B_0^2} \int d^3 x d^3 v \frac{\partial F_{\alpha}}{\partial E} \langle (\mu B + M v_{\parallel}) \kappa \cdot \xi \rangle^2 \frac{\omega_{\star}}{\langle \omega_d \rangle} \quad (18)$$

with δI given by

$$\delta I = \frac{\gamma}{\omega_A} \int d^3 x \xi^2. \quad (19)$$

Here δI comes from the inertial energy. Note that for small growth rate γ , there is no dependence on γ in δI as the main contribution to the integral comes from the $q=1$ layer. In Eq. (18), F_{α} is alpha particle distribution function, μ is magnetic moment, κ is magnetic curvature, ξ is plasma displacement for the kink mode, ω_{\star} and ω_d are alpha particle's diamagnetic drift frequency and magnetic drift frequency, respectively. Angular brackets represent bounce average over trapped particle's banana orbit.

In the limit of large aspect ratio, circular geometry and $1 - q(0) \ll 1$, δW_{α} can be written as¹³:

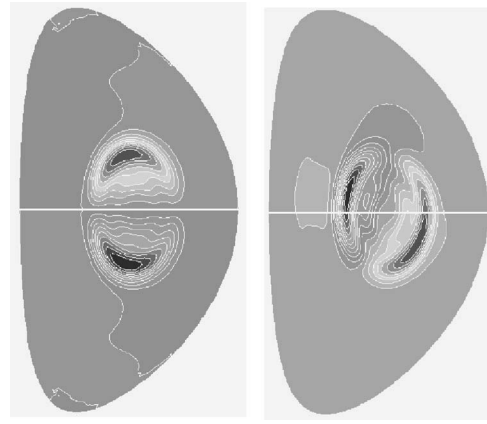


FIG. 2. The $n=1$ internal kink mode structure with (right) and without (left) alpha particles.

$$\delta W_{\alpha} = \delta W_{\alpha}^{\text{cir}} = - \frac{\sqrt{3}\pi}{8s_1} \sqrt{\frac{R}{r}} \int_0^{r_1} r dr \times \left[(0.6 + 3.2(1 - q - 0.5s)) \left(\frac{r}{r_1} \right)^{1.5} \frac{d\hat{p}_{\alpha}}{dr} \right] \quad (20)$$

where $r=r_1$ is the minor radius at which $q(r_1)=1.0$, s_1 is the magnetic shear at $r=r_1$, and \hat{p}_{α} is the alpha pressure normalized to unity at the center. This analytic result agrees well with our numerical results for a model tokamak equilibrium with circular flux surfaces.

We now consider the case of ITER. The main parameters and profiles, obtained from a TRANSP simulation,²⁹ are as follows: $B=5.05$ T, $R=620$ cm, $a=200$ cm, electron density $n_e(0)=1.0^{14}$ cm⁻³, $T_i(0)=19$ keV, $T_e(0)=23$ keV, central total beta $\beta(0)=6.5\%$, $\beta_{\alpha}(0)=1\%$, $q(0) \sim 0.9$, and $q(a)=3.83$. The alpha particle distribution is a slowing-down function given by Eq. (13). Using these parameters and profiles, linear simulations have been carried out to determine the alpha particle stabilization effects. Figure 2 shows the $n=1$ internal kink eigenmode structure with (right) and without (left) alpha particles. The MHD growth rate $\gamma_{\text{MHD}}/\omega_A=0.0070$ is reduced to $\gamma/\omega_A=0.0039$ with alpha particles, which corresponds to $\delta W_{\alpha}=0.31$. However, the simple analytic estimate in Eq. (20) gives $\delta W_{\alpha}=0.82$ which is much larger. We have shown analytically and numerically that this discrepancy is mainly due to the elongation of the ITER plasma shape. To illustrate the importance of this effect, Fig. 3 shows δW_{α} as a function of elongation at zero triangularity whereas all other parameters and profiles are fixed. We observe that the stabilization effects of alpha particles decreases as elongation increases. At the full ITER shape (elongation=1.8), alpha particle stabilization is reduced by a factor of 2.5 as compared to the circular shape case. This result shows that the elongation of plasma shape is an important factor for the alpha particle stabilization of the internal kink mode and it must be taken into account for realistic modeling of the internal kink stability and sawteeth in ITER.

We now give a brief derivation to show the effects of elongation found in our numerical study. We assume large

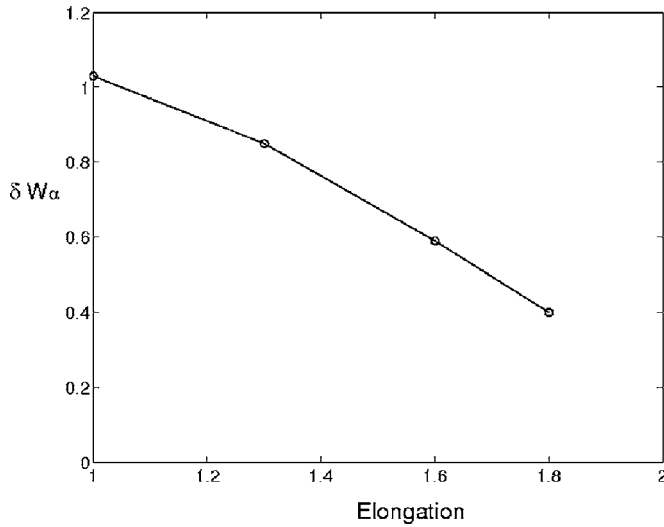


FIG. 3. The alpha particle stabilizing contribution δW_α as a function of elongation.

aspect ratio and low beta tokamak equilibria whose flux surfaces are described by

$$R = R_0 + r \cos(\theta), \quad (21)$$

$$Z = \kappa r \sin(\theta),$$

where κ is elongation and is a constant. Note that r is a flux variable. The Jacobian of this toroidal coordinates is $J = \kappa r R$. For simplicity, we have neglected Shafranov's shift and all other high order toroidicity terms. The plasma displacement for internal kink mode is almost incompressible and can be written as

$$\xi = R^2 \mathbf{b} \times \nabla u + \xi_\parallel \mathbf{b}, \quad (22)$$

where $u = u(r) \sin(\theta - \phi)$ with $u(r) = r$ for $q < 1$ and $u(r) = 0$ for $q > 1$.

Using Eq. (21), it can be shown easily that $\omega_\star \propto 1/\kappa$ and $\omega_d \propto 1/\kappa$. Thus, the elongation dependence of ω_\star cancels that of ω_d . However, the elongation dependence does enter the inertial term δI and the bounce averaged term $\langle (\mu B + M v_\parallel) \kappa \cdot \xi \rangle$ in δW_α . After some algebra, δW_α can be written as

$$\delta W_\alpha = \frac{2\sqrt{3}}{\sqrt{(1+\kappa^2)(5+\kappa^2)}} \delta W_\alpha^{\text{cir}}. \quad (23)$$

Note that for $\kappa=1$, Eq. (23) recovers the circular limit. For ITER parameters, we have $\kappa \sim 1.5$ near $q=1$ surface and δW_α is reduced by 30% from the circular limit. This analytic result agree qualitatively with our numerical results. A better quantitative agreement requires keeping the combined effects of elongation and toroidicity as well as shaping effects on mode structure and is beyond the scope of this article.

It should be pointed out that our results of shaping effects are significantly different from the previous results found by Wu *et al.*¹⁵ In fact, they found the elongation enhances the alpha particle stabilization. The discrepancy is partly due to the different coordinates used. Their results were obtained from an analytic dispersion relation which

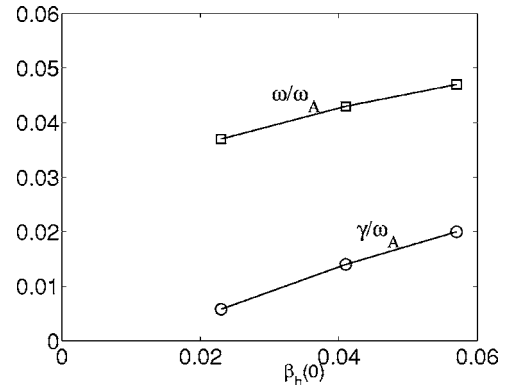


FIG. 4. The fishbone mode frequency and growth rate vs energetic particle beta.

showed δW_α is proportional to a weighted average of ω_\star/ω_d . In their coordinates, the plasma volume was kept fixed as elongation changes whereas in ours the plasma volume scales as elongation. Thus, they obtained $\omega_\star/\omega_d \sim (1+\kappa)/2$ whereas in our case ω_\star/ω_d is independent of κ . Using our coordinates, Wu *et al.* would found no elongation dependence of alpha particle stabilization. Instead, our new numerical and analytical results show a significant effect of elongation.

V. FISHBONE INSTABILITY

The fishbone instability was first discovered in the PDX tokamak. The name “fishbone” came from the characteristic shape of the magnetic signal from the Mirnov coils. It is basically an $(n, m) = (1, 1)$ internal kink mode destabilized by energetic trapped particles via precessional resonance. Here we use the M3D hybrid code to study the excitation and nonlinear evolution of the fishbone instability driven by energetic particles. In particular, we investigate the nonlinear dynamics of the instability.

We start with linear simulations. We consider a sequence of circular tokamak equilibria with increasing energetic particle pressure. The plasma parameters and profiles are the same as in Sec. III except the q profile is specified by $q_0=0.9$, $q_1=2.5$, $q'_0=0.78$, and $q'_1=5.0$ (this corresponds to a $q=1$ radius of $r_1/a \sim 0.5$). The energetic particle distribution is an isotropic slowing-down one given by Eq. (13) with $\rho_h/a=0.05$ and $v_0/v_A=1$. Figure 4 plots the fishbone growth rate and mode frequency versus energetic particle beta $\beta_h(0)$ from three cases: (A) $\beta_h(0)=2.6\%$, (B) $\beta_h(0)=4.3\%$, and (C) $\beta_h(0)=5.7\%$. The plasma thermal beta is very small, with $\beta_h/\beta_{\text{total}} \sim 0.9$ for all these cases. Figure 5 shows the velocity stream function U and the nonadiabatic part of perturbed energetic particle pressure δP_\parallel and δP_\perp of the linear eigenmode for case B. We observe that the eigenmode structure is mainly a $(1, 1)$ mode as expected. We also observe in Fig. 4 that the growth rate increases approximately linearly as a function of $\beta_h(0)$ whereas the mode frequency varies slightly about $\omega \sim 0.04$. This frequency is comparable to the nominal energetic particle precessional frequency $\omega_d/\omega_A \sim \frac{1}{2} k_\theta \rho_h v_h/v_A \sim 0.05$. These results are consistent with analytic results for the fishbone instability.

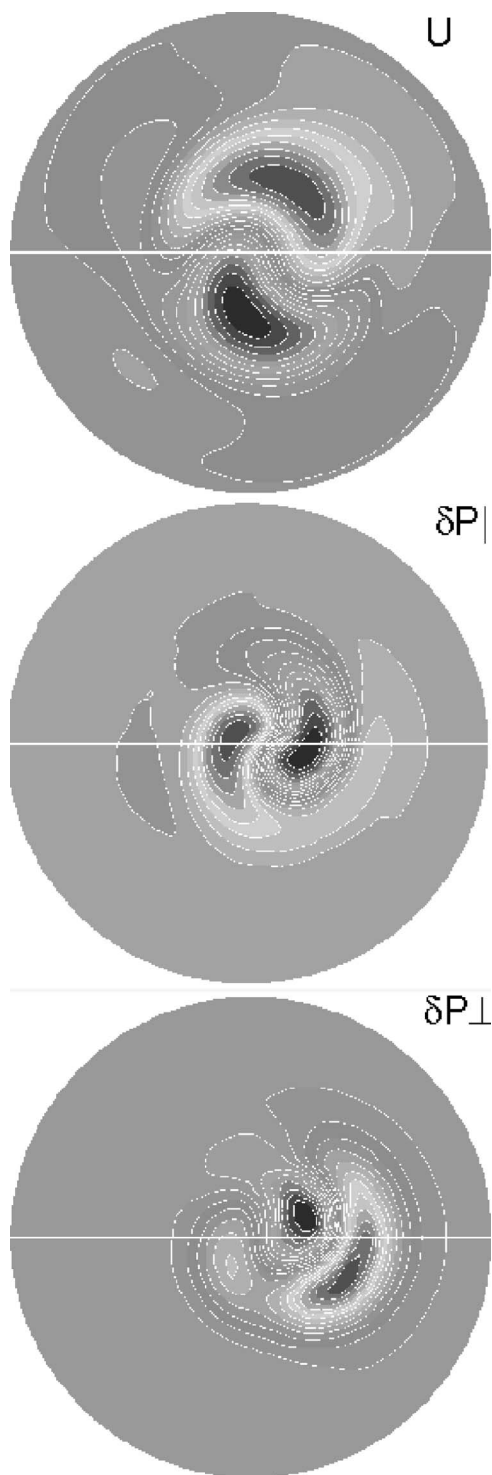


FIG. 5. The contours of the fishbone linear eigenmode for velocity stream function U and the perturbed energetic particle pressure $\delta P_{||}$ and δP_{\perp} .

We now turn to nonlinear simulation results. We first focus on the particle nonlinearity by imposing a linear MHD response from the thermal species. The MHD response is constrained to be linear by keeping only a single toroidal mode number in the perturbation. Figure 6 shows the nonlinear evolution of U_{\cos} (the $\cos \phi$ component of U) for cases A, B and C. Figure 7 shows the corresponding evolution of $\ln(|U|)$ where $|U| = \sqrt{U_{\cos}^2 + U_{\sin}^2}$ is the amplitude of U . We

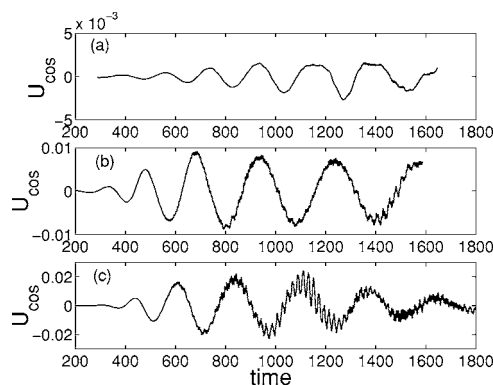


FIG. 6. Nonlinear evolution of the \cos component of U for case A (top), B (middle), and C (bottom).

observe that the mode first grows linearly (seen more clearly in Fig. 7) and then begins to saturate after a few oscillations. The initial saturation amplitude scales as $U_{\text{amp}} \sim \gamma^2$ as shown in Fig. 8. It is interesting to note that after the initial saturation, the mode amplitude can oscillate (case A with smallest growth rate), or decay slowly (case B) or decay rapidly (case C with largest linear growth rate). We also observe that the frequency of the mode chirps down significantly as the mode oscillation period increases for all these cases. This can be clearly seen in Fig. 9 where we plot the mode frequency versus time. We observe up to a factor of 2 reduction in mode frequency at the end the simulation runs. It should be pointed out that the calculated mode frequency is evaluated from the rate of phase change of U averaged over $\Delta t = 45$.

It is interesting to ask whether the mode structure changes significantly during the nonlinear evolution. Figure 10 plots contours of U at three times: $t=297$ (top, linear stage), $t=594$ (middle, initial saturation) and $t=1578$ (late stage of nonlinear evolution), for case B. We note that the mode structure at the initial saturation is similar to the linear eigenmode, but the mode structure changes significantly at later stage of the evolution. This is actually not surprising as the mode frequency has changed by a large amount by that time.

We now investigate the physical mechanism for saturation and mode frequency chirping. Figure 11 shows the evolution of the energetic particle distribution at particle speed

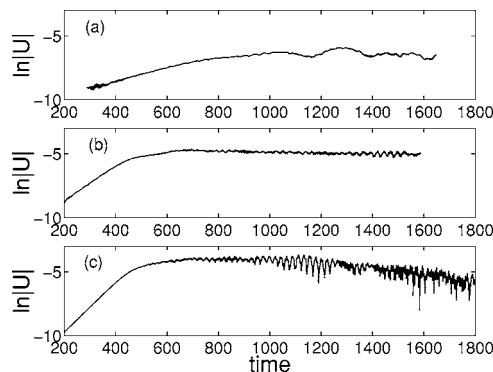
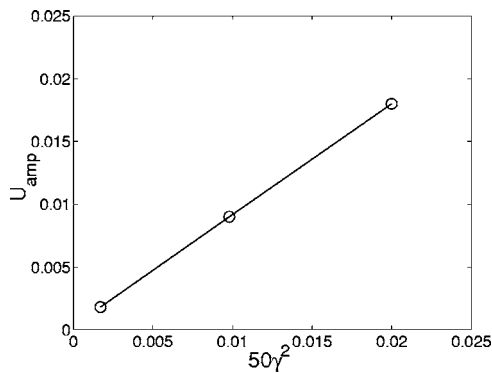


FIG. 7. The nonlinear evolution of the mode amplitude $\ln|U|$ for case A (upper), B (middle), and C (lower).

FIG. 8. The initial saturation amplitude of U vs $50\gamma^2$.

$v/v_A \sim 0.8$ and pitch angle $\Lambda = \mu B_0/E \sim 1.0$. Note that the horizontal axis P_ϕ corresponds to a radial variable ranging from -0.42 at the center of plasma to 0 at the plasma edge. We observe that the distribution becomes flattened starting from $t \sim 500$ when the mode frequency begins to chirp down rapidly. Further, the flattening region widens clearly from this time. Notice that the shoulder of the flattening region moves out radially in time. As the instability is driven by df/dP_ϕ , the initial saturation is caused by the nonlinear flattening of the distribution. On the other hand, the frequency chirping can be explained by the movement of the shoulder in the distribution function. In the nonlinear evolution, we expect the mode frequency evolves according to the distribution evolution in order to maximize instability drive. In particular, we expect that the maximum drive comes from the steep gradient region just outside the shoulder region. As the precession drift frequency of trapped particles at fixed energy and pitch angle is smaller for larger P_ϕ (or larger radius), the mode frequency needs to decrease in time as the

steep gradient region moves out radially in order to satisfy the resonant condition $\omega = \omega_d$ and tap the free energy associated with the df/dP_ϕ .

So far, we have neglected the MHD nonlinearity in the nonlinear simulations. We have also carried out simulations with both particle nonlinearity and MHD nonlinearity. Figure 12 compares fishbone amplitude evolutions with (dashed line) and without (solid line) MHD nonlinearity. The results are obtained for another fishbone case with $\omega/\omega_A = 0.078$ and $\gamma/\omega_A = 0.017$. We observe that the MHD nonlinearity reduces the initial saturation level. However, the MHD nonlinearity does not enhance the initial mode growth in contrast to the results of Odblom *et al.*²⁵ In the work of Odblom *et al.*, the MHD nonlinear enhancement of the initial mode growth was found near marginal stability when the linear mode had a double layer radial structure around the $q=1$ surface. In this work, however, the linear mode has a single layer structure around the $q=1$ surface due to finite numerical viscosity. Results of nonlinear cases with small viscosity will be reported in future.

A word on the numerical resolution is in order here. For the simulation results presented in this work, we typically used about 61 radial zones, 7000 mesh points in a poloidal plane, and 16 toroidal zones. Up to 8 million simulation particles have been used. It is found that this numerical resolution and particle number are sufficient for the cases considered earlier.

Compared to the previous work of Candy *et al.*,²⁴ the present work is more self-consistent and comprehensive. Candy *et al.* used a reduced model where the mode structures was assumed to be fixed and a simple dispersion relation for the fishbone mode was used to evolve the mode amplitude. In the work presented here, we used the full MHD equations together with energetic particle effects. The mode structure is

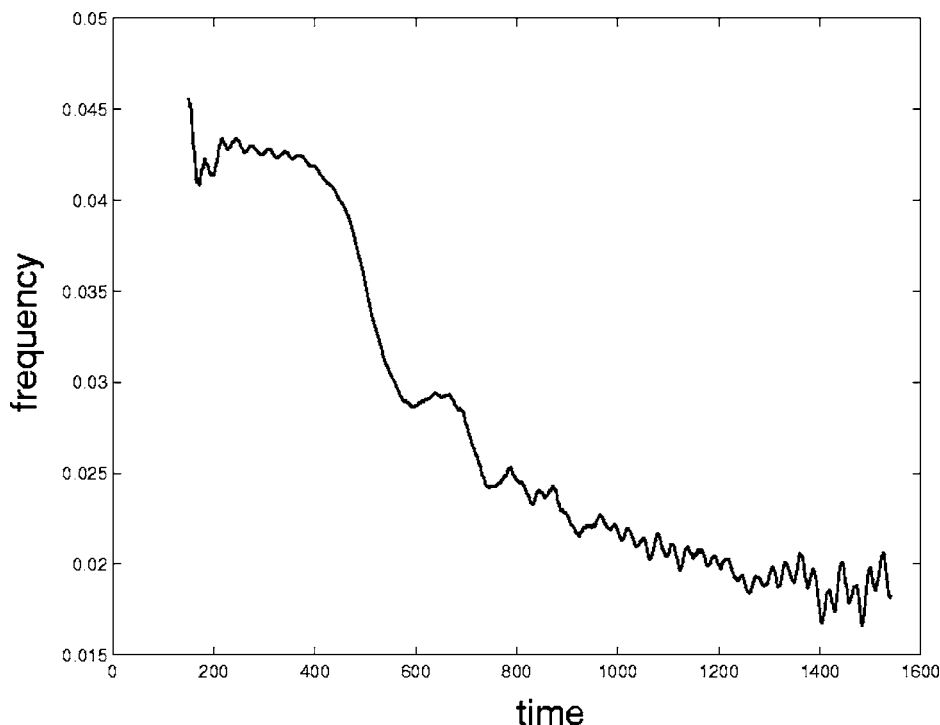


FIG. 9. The nonlinear evolution of the fishbone mode frequency for case B.

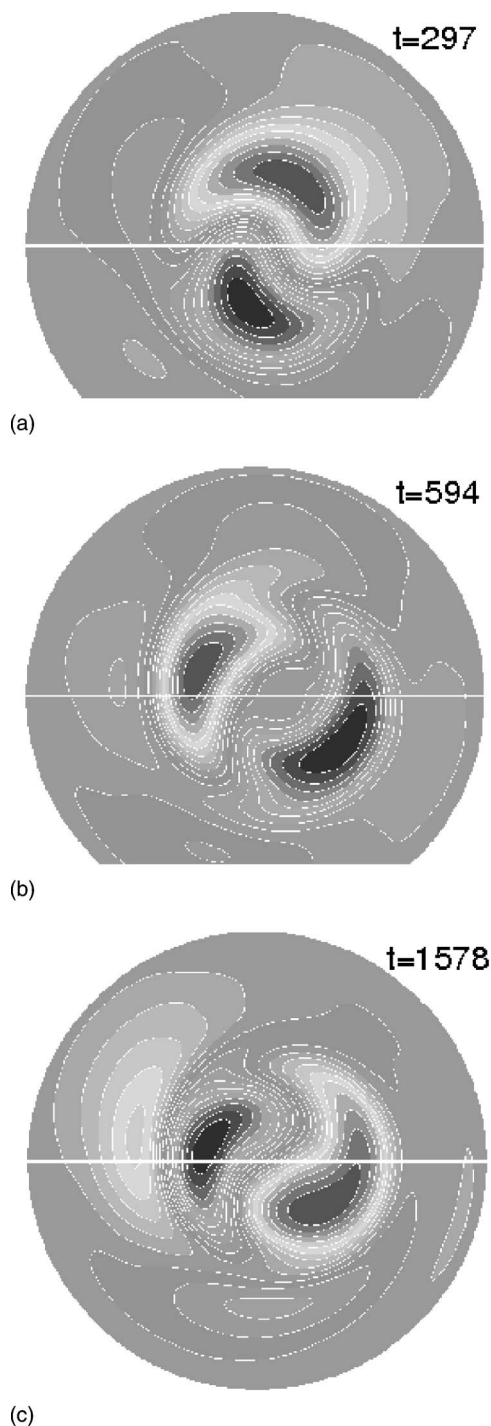


FIG. 10. The fishbone mode structure of U for case B at three time slices: (a) in linear stage at $t=297$, (b) near initial saturation at $t=594$, and (c) in late nonlinear stage at $t=1578$.

determined nonperturbatively with energetic particle effects. Our results agree with theirs in that we both find strong frequency chirping. However, our saturation levels are higher. For example, for the case A with lowest growth rate, the saturation level in terms of plasma radial displacement is around $\xi_r/a \sim 0.24$ (obtained without MHD nonlinearity). This corresponds to a displacement about half of the $q=1$ radius. However, a more careful quantitative comparison with the work of Candy *et al.* is not possible regarding satu-

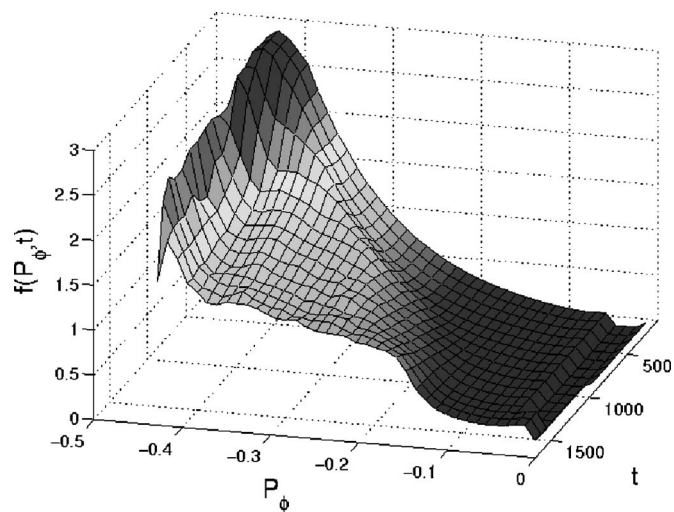


FIG. 11. The trapped particle distribution function vs time at $v/v_A=0.8$ and $\Lambda=1.0$.

ration level as simulation parameters used are fairly different. In particular, their linear growth rate appeared to be smaller than ours. This may explain why their saturation level is lower than ours. Also, it would be interesting to examine the role of nonperturbative mode structure on nonlinear saturation, but this is beyond the scope of this work.

Finally it should be pointed out that our results for the nonlinear fishbone is qualitatively similar to the hole-clump theory of the bump-in-tail instability by Berk *et al.*³⁰ In particular, the nonlinear frequency evolution in Fig. 10 approximately scales as $\delta f \sim \sqrt{t}$ as found analytically by their theory.

VI. CONCLUSIONS

We have performed global hybrid simulations of the $n=1$ internal kink mode in the presence of energetic particles using the M3D hybrid code. For ITER parameters and profiles, the effects of alpha particles are stabilizing. However, the elongation of ITER strongly reduces the alpha stabilization effects. Thus, shaping effects should be retained in the modeling of internal kink stability and related sawteeth oscillations for ITER. On the second topic of this work, we

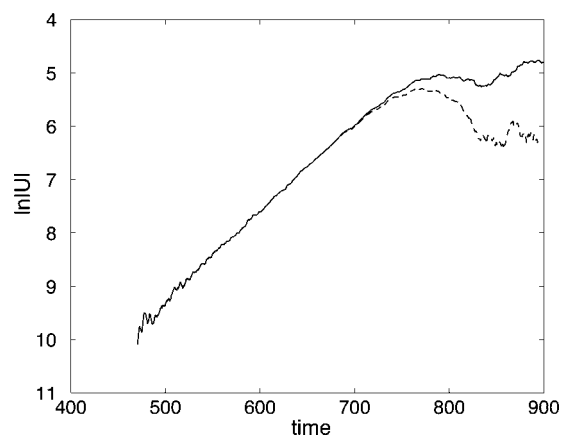


FIG. 12. The evolution of the mode amplitude $\ln|U|$ with (dashed line) and without (solid line) fluid nonlinearity.

have investigated the nonlinear dynamics of the fishbone instability in tokamaks. Our model is self-consistent, including both particle nonlinearity and MHD nonlinearity. The mode structure is nonperturbatively determined together with energetic particle effects. It is found that nonlinear flattening of the particle distribution function near the resonance region leads to mode saturation and strong downward frequency chirping. Thus, particle nonlinearity alone can account for the characteristic feature of experimental observations. The MHD nonlinearity reduces the initial saturation level.

ACKNOWLEDGMENTS

The authors are indebted to Dr. N. N. Gorelenkov who provided the NOVA2 results for the benchmark case and to Dr. R. Bundy who provided the parameters and profiles of ITER from the TRANSP code. They also would like to thank Dr. S. Ethier for showing them an efficient way of MPI for the particle parallelization and Dr. S. Klasky for help in AVS visualization.

This work was supported in part by U. S. DOE Contract No. DE-AC02-76-CHO3073. It was carried out as a part of the Center for Extended MHD Modeling (CEMM) project under SciDAC. The simulations were carried out using the massively parallel supercomputer Seaborg at NERSC.

APPENDIX A: COORDINATES, FIELD VARIABLES, AND DISCRETIZATION

The cylindrical coordinates (R, Z, ϕ) are used as the spacial coordinates for the M3D code. In this set of coordinates, the magnetic field and plasma velocity is written as

$$\mathbf{B} = \nabla \Psi \times \nabla \phi + \frac{1}{R} \nabla_{\perp} F + \frac{I}{\epsilon} \nabla \phi \quad (\text{A1})$$

and

$$\mathbf{v} = \epsilon R^2 \nabla u \times \nabla \phi + \nabla_{\perp} \chi + R v_{\phi} \nabla \phi, \quad (\text{A2})$$

where

$$\nabla_{\perp} = \nabla R \frac{\partial}{\partial R} + \nabla Z \frac{\partial}{\partial Z} \quad (\text{A3})$$

and $\epsilon = a/R_0$.

The time evolution equations are solved for nine independent variables Ψ , I , u , χ , v_{ϕ} , P , and ρ , P_{\parallel} , and P_{\perp} . Note that F is related to I from zero divergence of the magnetic field.

A linear triangle finite element method is used in the poloidal plane [i.e., in (R, Z) space] and a fourth-order finite difference method is used in toroidal direction.

APPENDIX B: δf METHOD

A δf method is used to reduce particle noise in hybrid simulations. In this method, the full particle distribution is written as $f = f_0 + \delta f$ where f_0 is the equilibrium distribution and δf is the perturbed one. We define a weight $w = \delta f/g$ where g is the distribution of loaded simulation particles (or markers). The evolution equation for the weight is

$$\frac{dw}{dt} = - \left(\frac{f}{g} - w \right) \frac{1}{f_0} \frac{df_0}{dt}. \quad (\text{B1})$$

The equilibrium distribution is expressed as a function of the constants of motion:

$$f_0 = f_0(P_{\phi}, E, \mu), \quad (\text{B2})$$

where P_{ϕ} is the toroidal angular momentum, E is the energy, and μ is the magnetic moment. Then

$$\frac{df_0}{dt} = \frac{dP_{\phi}}{dt} \frac{\partial f_0}{\partial P_{\phi}} + \frac{dE}{dt} \frac{\partial f_0}{\partial E}, \quad (\text{B3})$$

where

$$\frac{dE}{dt} = e \mathbf{v}_d \cdot \langle \mathbf{E} \rangle + M \mu \frac{d\langle \delta B \rangle}{dt}, \quad (\text{B4})$$

$$\frac{dP_{\phi}}{dt} = \left(\frac{d\mathbf{X}}{dt} \right)_1 \cdot \nabla P_{\phi} + \left(\frac{dv_{\parallel}}{dt} \right)_1 \frac{\partial P_{\phi}}{\partial v_{\parallel}}, \quad (\text{B5})$$

$$\left(\frac{d\mathbf{X}}{dt} \right)_1 = \frac{1}{B^{**}} \left[v_{\parallel} (\delta \mathbf{B} - \mathbf{b}_0 \times (\langle \delta \mathbf{E} \rangle - \frac{1}{e} \mu \nabla \langle \delta B \rangle)) \right], \quad (\text{B6})$$

$$m \left(\frac{dv_{\parallel}}{dt} \right)_1 = \frac{e}{B^{**}} \delta \mathbf{B} \cdot \left(\langle \mathbf{E} \rangle - \frac{1}{e} \mu \nabla (B_0 + \langle \delta B \rangle) \right) + \frac{e}{B_0^{**}} \mathbf{B}^* \cdot \left(\langle \delta \mathbf{E} \rangle - \frac{1}{e} \mu \nabla \langle \delta B \rangle \right), \quad (\text{B7})$$

where the subscript 1 denotes the perturbed part. In term of particle weight, the perturbed parallel and perpendicular pressure is given by

$$\begin{aligned} \delta P_{\parallel}(\mathbf{x}) &= \int M v_{\parallel}^2 \delta(\mathbf{x} - \mathbf{X} - \rho_{\mathbf{h}}) \\ &\times \left(w + \frac{\delta B^{**}}{B^{**}} \left(\frac{f}{g} - w \right) \right) B^{**} g d^3 \mathbf{X} dv_{\parallel} d\mu d\theta, \end{aligned} \quad (\text{B8})$$

$$\begin{aligned} \delta P_{\perp}(\mathbf{x}) &= \int \frac{1}{2} M v_{\perp}^2 \delta(\mathbf{x} - \mathbf{X} - \rho_{\mathbf{h}}) \\ &\times \left(w + \frac{\delta B^{**}}{B^{**}} \left(\frac{f}{g} - w \right) + \frac{\delta B}{B} \frac{f}{g} \right) \\ &\times B^{**} g d^3 \mathbf{X} dv_{\parallel} d\mu d\theta, \end{aligned}$$

APPENDIX C: PARTICLE CALCULATIONS WITH UNSTRUCTURED MESH

Here we briefly describe the numerical methods used in the particle part of the hybrid code. This part of code consists of three main steps: (a) particle loading; (b) particle pushing; and (c) calculations of P_{\parallel} and P_{\perp} . In the particle part, we use the same unstructured mesh and triangle elements as in the fluid part of the code. In order to push particles and to cal-

culate the particle pressure, it is essential to locate which triangle cell each particle is in. To aid particle search, we use an auxiliary set of coordinates (x, y, ϕ) in addition to the cylindrical coordinates (R, Z, ϕ) for particles. This set of (x, y, ϕ) is related to the flux coordinates (s, θ, ϕ) as follows:

$$\begin{aligned} x &= \sqrt{s} \cos(\theta), \\ y &= \sqrt{s} \sin(\theta), \end{aligned} \quad (\text{C1})$$

where s is chosen to be the normalized toroidal flux. We carry out particle search in this coordinates because the unstructured mesh is constructed based on the flux coordinates. Once (x, y, ϕ) is known for a particle, it is quite straightforward to determine which cell it is in.

First, we consider particle loading. In general we can use any marker distribution g . For convenience, we usually load particles uniformly in $(R, Z, \phi, v_{\parallel}, v_{\perp}^2)$ space. This corresponds to a marker distribution of $g = B/B^{**}$.

Second, we describe particle pushing. We use the Leap-Frog scheme to push particles according to Eq. (9). To do this, we need to evaluate fields at each particle position. For any field (e.g., B), the value at the particle location can be determined by

$$B(x, y, \phi) = \sum_{i,j} c_{i,j} B(i, j), \quad (\text{C2})$$

where $B(i, j)$ is the value of B at j th toroidal angle and i th vertex of the triangle cell in which the particle is located. The weight coefficients $c_{i,j}$ are determined by particle location (x, y, ϕ) . We advance each particle both in the cylindrical coordinates and the (x, y, ϕ) coordinates. The evolution equations for (R, Z, ϕ) follows directly from Eq. (9). The equations in (x, y, ϕ) coordinates can be obtained by using chain rule:

$$\begin{aligned} \frac{dx}{dt} &= \left(\frac{dR}{dt} - \frac{d\phi}{dt} \frac{\partial R}{\partial \phi} \right) \frac{\partial x}{\partial R} + \left(\frac{dZ}{dt} - \frac{d\phi}{dt} \frac{\partial Z}{\partial \phi} \right) \frac{\partial x}{\partial Z}, \\ \frac{dy}{dt} &= \left(\frac{dR}{dt} - \frac{d\phi}{dt} \frac{\partial R}{\partial \phi} \right) \frac{\partial y}{\partial R} + \left(\frac{dZ}{dt} - \frac{d\phi}{dt} \frac{\partial Z}{\partial \phi} \right) \frac{\partial y}{\partial Z}. \end{aligned} \quad (\text{C3})$$

Finally, the perturbed particle pressures can be determined straightforwardly by using Eq. (B8) and the weight coefficients as follows:

$$\begin{aligned} \delta P_{\parallel} &= \sum_k M v_{\parallel}^2 \left(w_k + \frac{\delta B^{**}}{B^{**}} \left(\frac{f_k}{g_k} - w_k \right) \right) c_{i,j} / dV_i, \\ \delta P_{\perp} &= \sum_k \frac{1}{2} M v_{\perp}^2 \left(w + \frac{\delta B^{**}}{B^{**}} \left(\frac{f}{g} - w \right) + \frac{\delta B}{B} \frac{f}{g} \right) c_{i,j} / dV_i \end{aligned} \quad (\text{C4})$$

in the limit of zero gyroradius. Here subscript k is the particle index and dV_i is the volume associated with the k th particle's triangle cell.

- ¹ITER Physics Basis Editors *et al.*, Nucl. Fusion **39**, 2137 (1999).
- ²W. Park, E. V. Belova, G. Y. Fu, X. Z. Tang, H. R. Strauss, and L. E. Sugiyama, Phys. Plasmas **6**, 1796 (1999).
- ³L. E. Sugiyama and W. Park, Phys. Plasmas **7**, 4644 (2000).
- ⁴G. Y. Fu and W. Park, Phys. Rev. Lett. **74**, 1594 (1995).
- ⁵G. Y. Fu, J. Chen, S. Jardin, W. Park, H. R. Strauss, and L. E. Sugiyama, Bull. Am. Phys. Soc. **47**, 115 (1992).
- ⁶G. Y. Fu, J. Breslau, E. Fredrickson, W. Park, and H. R. Strauss, Proceedings of the 2004 IAEA Fusion Energy conference, Vilamoura, Portugal, 2004, paper TH/P4-38.
- ⁷H. R. Strauss, L. E. Sugiyama, G. Y. Fu, W. Park, and J. Breslau, Nucl. Fusion **44**, 1008 (2004).
- ⁸J. W. Van Dam, M. N. Rosenbluth, and Y. C. Lee, Phys. Fluids **25**, 1349 (1982).
- ⁹F. Porcelli, Plasma Phys. Controlled Fusion **33**, 1601 (1991).
- ¹⁰R. B. White, L. Chen, F. Romanelli, and R. Hay, Phys. Fluids **28**, 278 (1985).
- ¹¹B. Coppi, R. J. Hastie, S. Migliuolo, F. Pegoraro, and F. Porcelli, Phys. Lett. A **132**, 267 (1988).
- ¹²R. O. Dendy, R. J. Hastie, K. G. McClements, and T. J. Martin, Phys. Plasmas **2**, 1623 (1995).
- ¹³K. G. McClements, R. O. Dendy, C. G. Gimblett, R. J. Hastie, and T. J. Martin, Nucl. Fusion **35**, 1761 (1995).
- ¹⁴C. Z. Cheng, Phys. Rep. **211**, 1 (1992).
- ¹⁵Y. Wu, C. Z. Cheng, and R. B. White, Phys. Plasmas **1**, 3369 (1994).
- ¹⁶J. P. Graves, O. Sauter, and N. N. Gorelenkov, Phys. Plasmas **10**, 1034 (2003).
- ¹⁷K. McGuire, R. Goldston, M. Bell *et al.*, Phys. Rev. Lett. **50**, 891 (1983).
- ¹⁸L. Chen, R. B. White, and M. N. Rosenbluth, Phys. Rev. Lett. **52**, 1122 (1984).
- ¹⁹B. Coppi and F. Porcelli, Phys. Rev. Lett. **57**, 2272 (1985).
- ²⁰E. Fredrickson, L. Chen, and R. White, Nucl. Fusion **43**, 1258 (2003).
- ²¹R. Betti, Plasma Phys. Controlled Fusion **35**, 941 (1993).
- ²²B. Coppi, S. Migliuolo, and F. Porcelli, Phys. Fluids **31**, 1630 (1988).
- ²³W. W. Heidbrink *et al.*, Phys. Fluids B **5**, 2176 (1993).
- ²⁴J. Candy, H. L. Berk, B. N. Breizman, and F. Porcelli, Phys. Plasmas **6**, 1822 (1999).
- ²⁵A. Odblom, B. N. Breizman, S. E. Sharapov, T. C. Hender, and V. P. Pastukhov, Phys. Plasmas **9**, 155 (2001).
- ²⁶S. Briguglio, G. Vlad, F. Zonca, and C. Kar, Phys. Plasmas **2**, 3711 (1995).
- ²⁷Y. Todo and T. Sato, Phys. Plasmas **5**, 1321 (1998).
- ²⁸C. Z. Cheng, Phys. Fluids B **3**, 2463 (1991).
- ²⁹R. Budny (private communication, 2002).
- ³⁰H. L. Berk, B. N. Breizman, and J. Candy, M. Pekker, and N. V. Petviashili, Phys. Plasmas **6**, 3102 (1999).